Supporting Information for:

Second Harmonic Generation Studies of Fe(II) Interactions with Hematite (α-Fe_2O_3)

David S. Jordan,[a] Christopher J. Hull,[a] Julianne M. Troiano,[a] Shannon C. Riha,[b] Alex B.F. Martinson,[b] Kevin M. Rosso,[c] and Franz M. Geiger [a]*

[a]Department of Chemistry, Northwestern University, 2145 Sheridan Road, Evanston, IL 60208

[b]Argonne-Northwestern Solar Energy Research (ANSER) Center and Materials Science Division, Argonne National Laboratory, Argonne, IL 60439

[c]Chemical & Materials Sciences Division, Pacific Northwest National Laboratory, Battelle Boulevard, K1-83, Richland, Washington 99354

*Corresponding author: geigerf@chem.northwestern.edu

I. Salt Screening Isotherms

Typically, when SHG salt screening isotherms are measured at a pH above the PZC, one observes a decrease in the SHG signal intensity with increasing salt concentrations. Conversely, when a salt screening isotherm is performed at a pH below the PZC, the SHG signal intensity increases with increasing salt concentration. This has been explained to be due to the relative phase of the $\chi^{(2)}$ term and the $\chi^{(3)}$ term.[1] Above the PZC, constructive interference between the $\chi^{(2)}$ and $\chi^{(3)}$ terms leads to relatively large signal intensity, and, as the salt concentration is increased, the depth of the electric double layer decreases and fewer water molecules contribute to the SHG signal intensity via the $\chi^{(3)}$ term, and the total SHG signal decreases. Below the PZC, the $\chi^{(2)}$ and $\chi^{(3)}$ terms deconstructively interfere with each other. As the salt concentration increases, the magnitude of the $\chi^{(3)}$ decreases, but this causes less deconstructive interference between the two tensors and the total SHG signal intensity then increases.

We performed salt screening isotherms above and below the PZC for the hematite/water system. Above the PZC, the salt screening isotherm shows the typical decrease in SHG signal intensity with increasing salt concentration, consistent with the previously described mechanism. However, the salt screening isotherm that we performed below the PZC also shows a decrease in SHG signal with increasing salt concentration. This finding is rationalized here by invoking the optical properties of the hematite thin film. A UV-vis absorption spectrum (Figure S1) shows that the hematite thin film absorbs light in the 200 – 500 nm region. We note that the UV-vis spectrum present here of our 10-nm thin hematite films is somewhat different from that of the 30 nm-thick films published by Lian and coworkers.[2] We also note that Hupp and coworkers[3] have shown that the spectral features of hematite films become more defined as the iron oxide film thickness is increased, and that a 15 nm sample synthesized using the same ALD procedure used in this work produces a UV-vis spectrum that is similar to the one shown by Lian and workers. The wavelength of the SHG signal was 300 ± 5 nm throughout our experiments, and therefore the hematite itself is on resonance with the SHG signal. Specifically, at 300 ± 5 nm we are probing the edge of a ligand to metal charge transfer band.[4] Not only are $\chi^{(2)}$ and $\chi^{(3)}$ of the interfacial system contributing to the overall SHG signal intensity, but we now must consider an additional resonant term due to the hematite thin film, a term we define as ${}_{Fe}\chi^{(2)}$, that is contributing to the SHG signal. It should be noted that only the $\chi^{(3)}$ term is affected by changes in salt concentration and pH, assuming the salt used does not specifically adsorb to the interface. Therefore throughout this discussion, both $\chi^{(2)}$ and ${}_{Fe}\chi^{(2)}$ remain constant in both magnitude and direction.

To explain the decrease in SHG signal in the salt screening isotherm measured below the PZC in the hematite system (pH 4), we contest that the ${}_{Fe}\chi^{(2)}$ term constructively interferes with

the $\chi^{(3)}$ term below the PZC. The $\chi^{(2)}$ and $\chi^{(3)}$ terms must deconstructively interfere with one another, as previously described, however, the sum of the ${}_{Fe}\chi^{(2)}$ and the $\chi^{(3)}$ terms in this scenario is greater than the $\chi^{(2)}$ term. Therefore, any decrease in $\chi^{(3)}$ due to increasing salt concentration results in a decrease in the overall SHG signal intensity due to the presence of the ${}_{Fe}\chi^{(2)}$ term. This also holds above the PZC. In this case, the $\chi^{(2)}$ and $\chi^{(3)}$ terms constructively interfere, and the ${}_{Fe}\chi^{(2)}$ term deconstructively interferes with both $\chi^{(2)}$ and $\chi^{(3)}$. However, the sum of $\chi^{(2)}$ and $\chi^{(3)}$ is greater than the ${}_{Fe}\chi^{(2)}$ term, and as the salt concentration is increased, this results in a decrease in the $\chi^{(3)}$ term and a corresponding decrease in the SHG signal intensity. This is depicted in Figure S2 using one-dimensional vectors.

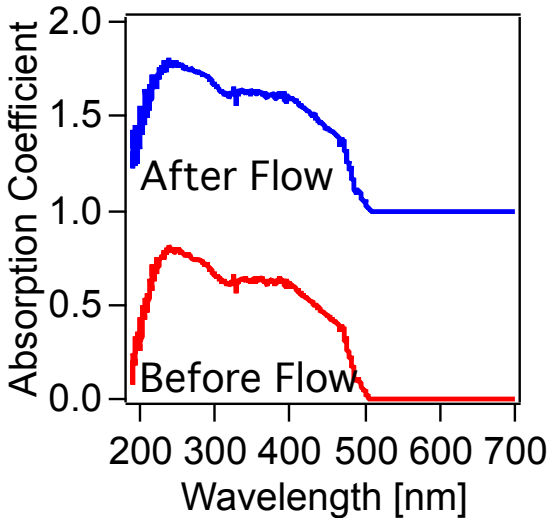

Figure S1 – UV-vis absorption spectrum for a 10 nm hematite thin film deposited onto a fused silica substrate before and after flowing a pH 4, 10 mM NaCl electrolyte solution for several hours.

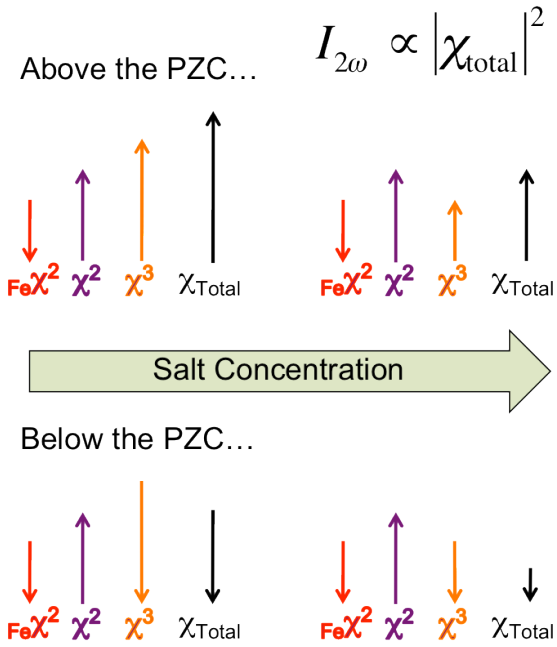

Figure S2 – Vector description of the contributing nonlinear susceptibility tensors to the overal SHG signal. Above the PZC, the $\chi^{(2)}$ and $\chi^{(3)}$ terms constructively interfere, while the ${}_{Fe}\chi^{(2)}$ is opposite in phase to both terms. Below the PZC, the $\chi^{(2)}$ and $\chi^{(3)}$ terms deconstructively interfere while the ${}_{Fe}\chi^{(2)}$ constructively interferes with the $\chi^{(3)}$ term. Therefore, any decrease in $\chi^{(3)}$ due to an increase in salt concentration results in a decrease in SHG signal intensity whether the system is above or below the PZC. It should be noted that the SHG signal cannot be negative and is proportional to the square modulus of the tensor sum.

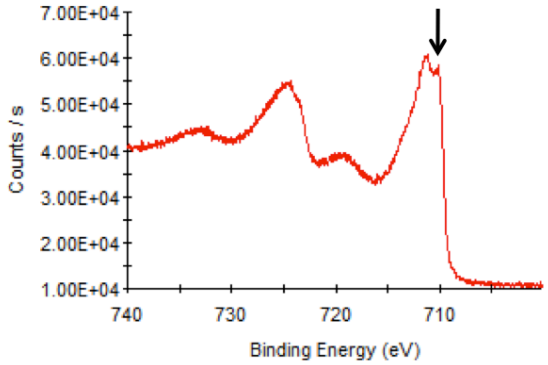

Figure S3 – A high-resolution scan of the Fe2p region shows a small step in the low energy side of the Fe $2p_{3/2}$ peak (indicated by arrow), characteristic of α-Fe_2O_3, specifically.

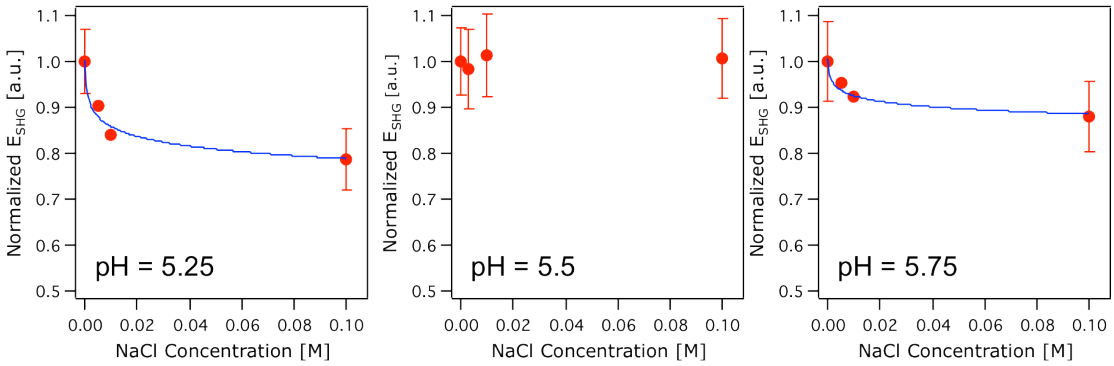

Figure S4 – SHG salt screening experiments performed on the hematite/water interface at the pH values indicated in the figure. The SHG E-field is invariant with increasing salt concentration at the PZC (represented by the middle plot at pH 5.5). As the solution pH is varied from the PZC, a change in SHG E-field with increasing salt is observed, indicating that there is a nonzero charge at the interface. The blue lines represent the fit of the data to the Gouy-Chapman model.

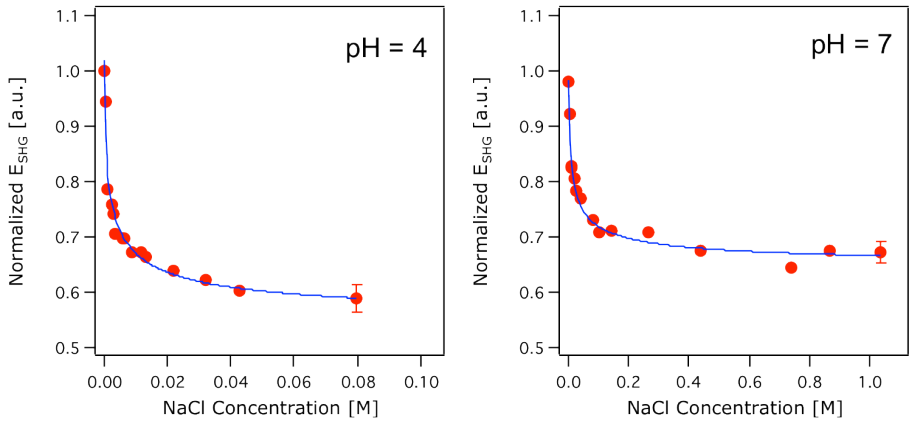

Figure S5 – SHG salt screening experiments performed at the hematite/water interface at pH 4 and 7. The blue line represents the fit of the data to the Gouy-Chapman model.

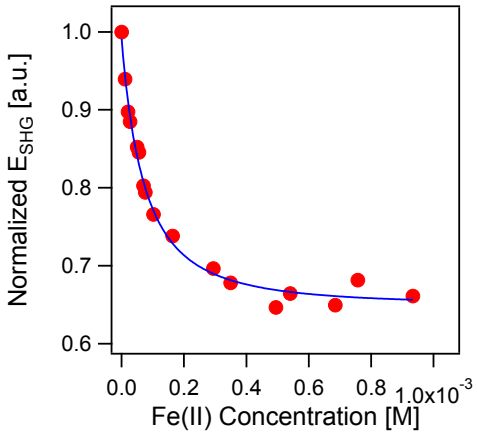

Figure S6 – SHG adsorption isotherm for Fe(II) binding to the fused silica surface at pH 4 and in 1 mM NaCl. The blue line represents the fit of the Gouy-Chapman model to the experimental data. The derived thermodynamic binding parameters are K_{ads} = 31,000 ± 4,000 M^{-1}, ΔG_{ads} = –39.6(4) kJ/mol, and σ_m = 0.0043(5) C/m^2.

Table S1 – Fit parameters for the Fe $2p_{3/2}$ multiplet fit. BE represents Binding Energy (in eV), CPS is counts per second, FWHM is full-width half maximum (in eV), and L/G mix is the Lorentzian/Gaussian ratio.

Name	Start BE	Peak BE	End BE	Height (CPS)	FWHM (eV)	Area (P) CPS.eV	area ratio	L/G mix (%)
Fe2p Scan A	716.28	709.78	706.78	6594.27	0.92	7252.42	1	80
Fe2p Scan B	716.28	710.65	706.78	4131.49	1.26	6237.08	0.86	80
Fe2p Scan C	716.28	711.33	706.78	3690.18	1.07	4714.07	0.65	80
Fe2p Scan D	716.28	712.26	706.78	2065.63	1.26	3118.54	0.43	80
Fe2p Scan E	716.28	713.23	706.78	1662.69	2.08	4133.88	0.57	80

Table S2 – Raman modes (in cm^{-1}) for different Fe_2O_3 phases and other iron oxide materials.[5-15]

α–Fe_2O_3	**γ–Fe_2O_3**	**Fe_3O_4**	**δ–FeOOH**
225	350	298	655
247	500	320	
293	700	420	
299		550	
412		669	
498			
613			
664 (surface disorder)			

Table S3 – Tabulated selected 2θ positions and peak intensities for several common iron oxides along with the miller indices for each feature (all data compiled from the respective PDF of each material).

Material/PDF	**2θ**	**Intensity**	**[hkl]**
α–Fe_2O_3	33.1523	100	[104]
00-033-0664	35.6112	70	[110]
	39.2756	3	[006]
	40.8544	20	[113]
	43.5177	3	[202]
	49.4791	40	[024]
	54.0892	45	[116]
	56.1504	1	[211]
	57.4276	5	[122]
	57.5886	10	[018]
	62.449	30	[214]
	63.9891	30	[300]
	66.0259	1	[125]
	69.5989	3	[208]
γ–Fe_2O_3	30.2406	35	[220]
00-039-1346	32.1244	2	[221]
	33.882	2	[310]
	35.6302	100	[311]
	37.2492	3	[222]
	38.8469	1	[320]
	40.3767	1	[321]
	43.2835	16	[400]
	44.7034	1	[410]
	46.0712	1	[330]
	50.007	2	[421]
	53.7326	10	[422]
	54.9243	1	[430]
	56.1056	1	[510]
	57.2714	24	[511]
	59.5681	1	[520]

	60.6848	2	[521]
	62.9251	34	[440]
	63.9942	1	[441]
	65.072	1	[530]
	67.2016	1	[442]
	69.2525	1	[610]
	69.305	1	[611]
Fe_3O_4	30.1465	30	[220]
01-071-6336	35.5092	100	[311]
	37.1445	8	[222]
	43.1566	20	[400]
	47.2526	1	[331]
	53.5422	8	[422]
	57.077	27	[511]
	62.6787	35	[440]
	65.9045	1	[531]
	66.9616	0	[442]

II. References

(1) Higgins, S. R.; Stack, A. G.; Knauss, K. G.; Eggleston, C. M.; Jordan, G. Probling molecular-scale adsorption and dissolution-growth processes using nonlinear optical and scanning probe methods suitable for hydrothermal applications. In *Water-Rock Interactions, ore deposits, and environmental geochemistry: A tribute to David A. Crerar*; Hellmann, R., Wood, S. A., Eds.; Special Publication No. 7; The Geochemical Society, 2002.

(2) Huang, Z.; Lin, Y.; Xiang, X.; Rodriguez-Cordoba, W.; McDonald, K. J.; Hagen, K. S.; Choi, K.-S.; Brunschwig, B. S.; Djamaladdin, G. M.; Hill, C. L.; Wang, D.; Lian, T. *Energy & Environmental Science* **2012**, *5*, 8923.

(3) Martinson, A. B. F.; DeVries, M. J.; Libera, J. A.; Christensen, S. T.; Hupp, J. T.; Pellin, M. J.; Elam, J. W. *J. Phys. Chem. C* **2011**, *115*, 4333.

(4) Sherman, D. M.; Waite, T. D. *American Mineralogist* **1985**, *70*, 1262

(5) Boucherit, N.; Delichere, P.; Joiret, S.; Hugot-Le Goff, A. *Mater. Sci. Forum* **1989**, *44-45*, 51

(6) Boucherit, N.; Hugot-Le Goff, A.; Joiret, S.; Beranger, G.; Chaudanson, H. *Thin Solid Films* **1989**, *174*, 111

(7) Chernyshova, I. V.; Hochella, M.; Madden, A. *Phys Chem Chem Phys* **2007**, *9*, 1736

(8) de Faria, D.; Venancio Silva, S.; de Oliveira, M. *Journal of Raman Spectroscopy* **1997**, *28*, 873.

(9) Garcia-Lobato, M.; Martinez, A.; Castro-Roman, M.; Falcony, C.; Escobar-Alarcon, L. *Physica B - Condensed Matter* **2011**, *406*, 1496.

(10) Klahr, B.; Martinson, A. B. F.; Hamann, T. *Langmuir* **2011**, *27*, 461.

(11) Lopez, L.; Pasteris, J.; Biswas, P. *Applied Spectroscopy* **2009**, *63*, 627.

(12) Mantovan, R.; Vangelista, S.; Cocco, S.; Lamperti, A.; Salicio, O. *J Appl Phys* **2012**, *111*, 07B107.

(13) Sartoretti, C.; Alexander, B.; Solarska, R.; Rutkowska, W.; Augustynski, J.; Cerny, R. *J Phys Chem B* **2005**, *109*, 13685.

(14) Tamm, A.; Dimri, M.; Kozlova, J.; Aidla, A.; Tatte, T.; Arroval, T.; Maeorg, U.; Mandar, H.; Stern, R.; Kukli, K. *Jounal of Crystal Growth* **2012**, *343*, 21.

(15) Vikulov, V.; Balashev, V.; Pisarenko, T.; Dimitriev, A.; Korobstov, V. *Technical Physics Letters* **2012**, *38*, 336.